



# Hetero phase modulated hematite photoanodes for practical solar water splitting

Cheng Lu<sup>a</sup>, Duo Zhang<sup>b</sup>, Zhenyu Wu<sup>a</sup>, Xiaoquan Zhao<sup>a</sup>, Kun Feng<sup>a</sup>, Gaoteng Zhang<sup>a</sup>, Shuao Wang<sup>b</sup>, Zhenhui Kang<sup>a,c,\*</sup>, Jun Zhong<sup>a,\*\*</sup>

<sup>a</sup> Institute of Functional Nano and Soft Materials Laboratory (FUNSOM), Jiangsu Key Laboratory of Advanced Negative Carbon Technologies, Soochow University, Suzhou 215123, China

<sup>b</sup> State Key Laboratory of Radiation Medicine and Protection, School of Radiation Medicine Protection, Soochow University, Suzhou 215123, China

<sup>c</sup> Macao Institute of Materials Science and Engineering (MIMSE), MUST-SUDA Joint Research Center for Advanced Functional Materials, Macau University of Science and Technology, Taipa 999078, Macao Special Administrative Region of China, China

## ARTICLE INFO

### Keywords:

Hematite  
Hetero phase  
Oxygen vacancy  
Solar water splitting  
Bulk charge utilization

## ABSTRACT

Hematite is an excellent catalyst for solar water splitting but its practical performance is still low. In this work, a hetero phase of  $\beta\text{-Fe}_2\text{O}_3$  was firstly introduced in  $\alpha\text{-Fe}_2\text{O}_3$  to optimize the internal structure, which can synergistically work with oxygen vacancy to enhance the charge extraction, facilitate the charge transport, and suppress the electron-hole recombination. As a result, the obtained hematite exhibits a high initial photocurrent of  $2.72\text{ mA/cm}^2$  at  $1.23\text{ V}$  vs. RHE, and can be well coupled with various further modifications such as P, Hf, and FeNiOOH to achieve an excellent photocurrent of  $5.24\text{ mA/cm}^2$  at  $1.23\text{ V}$  vs. RHE with a good stability over 100 h. Moreover, it can realize a benchmark solar-to-hydrogen conversion efficiency of 5.3% when connected to a commercial Si solar cell. The low cost, efficient, and stable hematite-based photoanodes may pave the way for practical solar water splitting.

## 1. Introduction

Hematite is an excellent catalyst for photoelectrochemical (PEC) solar water splitting due to its low cost, non-toxicity, good stability and suitable band gap width (1.9–2.2 eV) [1–5]. The theoretical solar-to-hydrogen (STH) conversion efficiency of hematite can be a high value around 15% [6,7]. Unfortunately, the practical PEC performance of hematite is far away from the theoretical value due to many factors [1–5]. Hematite typically requires for a suitable thickness to access an efficient light absorption, while the charge transport from bulk to surface will suffer from quick electron-hole recombination due to the poor conductivity and the presence of various bulk defects. Moreover, the surface/interface defects can also act as recombination centers and the final oxygen evolution reaction (OER) kinetics is very poor [2–5]. All these factors significantly hinder the high PEC performance of hematite for solar water splitting. In the last decades, the surface defects had been well modified by various methods and the OER kinetics could be significantly enhanced by using co-catalysts [8–24]. However, an

effective way for the important bulk charge utilization in hematite to achieve high performance, including charge transport, recombination, and extraction, is still a great challenge.

Doping in hematite is a main method to improve the bulk charge transport in hematite [5,10–16,25]. However, various doped elements in hematite may conflict between each other and then weaken the accumulated positive effects, resulting in a limited enhancement [10]. The creation of oxygen vacancies in hematite, named “intrinsic doping”, can effectively improve the bulk conductivity without the introduction of external elements, which is favorable for further modifications [18–23,26]. However, the process to create oxygen vacancies will typically produce more defects in the bulk or near surface regions, leading to a high onset potential [19,21]. Then the corresponding PEC performance of hematite with oxygen vacancies is still unsatisfied. New intrinsic methods to improve the bulk charge utilization should thus be developed.

Here we show an effective way to intrinsically improve the bulk charge utilization of hematite by creating hetero crystal phases.

\* Corresponding author at: Institute of Functional Nano and Soft Materials Laboratory (FUNSOM), Jiangsu Key Laboratory of Advanced Negative Carbon Technologies, Soochow University, Suzhou 215123, China.

\*\* Corresponding author.

E-mail addresses: [zhkang@suda.edu.cn](mailto:zhkang@suda.edu.cn) (Z. Kang), [jzhong@suda.edu.cn](mailto:jzhong@suda.edu.cn) (J. Zhong).

<https://doi.org/10.1016/j.apcatb.2023.122695>

Received 2 February 2023; Received in revised form 21 March 2023; Accepted 25 March 2023

Available online 27 March 2023

0926-3373/© 2023 Elsevier B.V. All rights reserved.

Different from the normal phase of  $\alpha$ - $\text{Fe}_2\text{O}_3$  in hematite,  $\beta$ - $\text{Fe}_2\text{O}_3$  or  $\gamma$ - $\text{Fe}_2\text{O}_3$  can also be produced in the sample to adjust the internal structure without external elements [27]. Hetero phases were reported to create abundant interfacial structures and show synergistic effect for better catalytic performance [28], which might facilitate the PEC performance of hematite. To the best of our knowledge, the controlled introduction of hetero phases in hematite has never been reported

before.

By controlling the temperature and pressure,  $\beta$ - $\text{Fe}_2\text{O}_3$  was successfully created in hematite along with the formation of oxygen vacancy. Oxygen vacancy has been proved to improve the conductivity, while the presence of  $\beta$ - $\text{Fe}_2\text{O}_3$  plays a key role to reduce the bulk (and/or near surface) defects and lower the onset potential. The hetero phase and oxygen vacancy in hematite can synergistically work to facilitate the

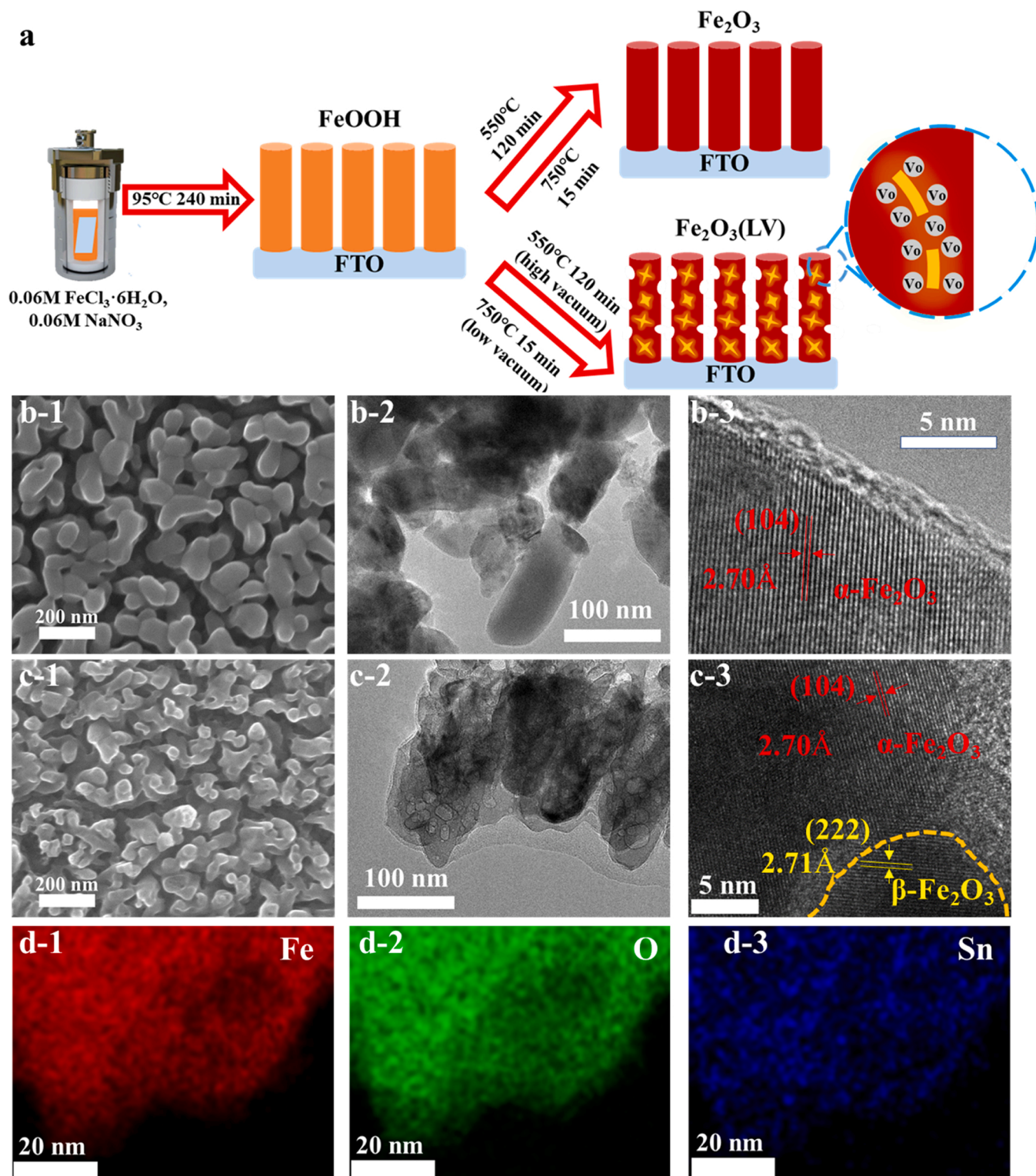


**Fig. 1.** Preparation process and morphology of  $\text{Fe}_2\text{O}_3$  (LV). (a) Experimental illustration for the preparation of  $\text{Fe}_2\text{O}_3$  and  $\text{Fe}_2\text{O}_3$  (LV). (b,c) SEM, TEM and HRTEM images of  $\text{Fe}_2\text{O}_3$  (b) and  $\text{Fe}_2\text{O}_3$  (LV) (c), respectively. (d-f) Dark field elemental mappings of  $\text{Fe}_2\text{O}_3$  (LV): Fe (d), O (e) and Sn (f).

charge transport, suppress the electron-hole recombination, and even enhance the charge extraction. As a result, the obtained photoanode can achieve an excellent initial photocurrent density of  $2.72 \text{ mA/cm}^2$  at  $1.23 \text{ V}$  vs. RHE, which is 3.3 times of that for the pristine hematite. Due to the favorable intrinsic modification property, the resulted hematite can be used as a good starting material for further treatments such as P (phosphorus), Hf (hafnium) and  $\text{FeNiOOH}$ . All the treatments can be well coupled to achieve a final high photocurrent of  $5.24 \text{ mA/cm}^2$  at  $1.23 \text{ V}$  vs. RHE, with a good stability over 100 h and the Faradaic efficiencies around 95%. Moreover, the photoanode can be directly connected to a commercial Si solar cell to form a tandem system, which can realize a benchmark STH efficiency of 5.3% ( $4.7 \text{ mA/cm}^2$  in the system) with the sunlight as the sole energy source. To the best of our knowledge, it represents the highest STH value for hematite-based solar water splitting systems ever reported in literature. The low cost, efficient, and stable hematite-based photoanodes with an easy tandem system might be used for the practical solar water splitting in the near future.

## 2. Experimental section

### 2.1. Chemicals and reagents

Iron(III) chloride hexahydrate ( $\text{FeCl}_3 \cdot 6\text{H}_2\text{O}$ , 99.0%), sodium nitrate ( $\text{NaNO}_3$ , 99.0%), sodium hydroxide ( $\text{NaOH}$ , 96%), phosphoric acid ( $\text{H}_3\text{PO}_4$ , 85%), hydrochloric acid ( $\text{HCl}$ , 36~38%), Nickel(II) chloride hexahydrate ( $\text{NiCl}_2 \cdot 6\text{H}_2\text{O}$ , 99.0%) and anhydrous ethanol were bought from Sinopharm Chemical Reagent Co., Ltd. Hafnium(IV) chloride ( $\text{HfCl}_4$ , 99%) was purchased from Shanghai Macklin Biochemical Co., Ltd. All the reagents were analytical grade and used as received without further purification. De-ionized water was obtained from an ultra-pure purifier (resistivity  $\geq 18.2 \text{ M}\Omega$ ).

### 2.2. Synthesis of $\text{Fe}_2\text{O}_3$

The pristine  $\text{Fe}_2\text{O}_3$  photoanode was prepared by a modified hydrothermal method [4,16,29]. In short, by using  $\text{FeCl}_3 \cdot 6\text{H}_2\text{O}$  as the precursor,  $\text{FeOOH}$  was grown on fluorine-doped  $\text{SnO}_2$  (FTO) substrate in a hydrothermal process at  $95^\circ\text{C}$  for 4 h. Then the sample was sintered in a muffle furnace (on a flat platform to withstand a high temperature) in air at  $550^\circ\text{C}$  for 2 h, with a further annealing at  $750^\circ\text{C}$  for 15 min (Fig. 1a) [4].

### 2.3. Synthesis of $\text{Fe}_2\text{O}_3$ (LV)

For the  $\text{Fe}_2\text{O}_3$  photoanode with oxygen vacancy and  $\beta\text{-Fe}_2\text{O}_3$ ,  $\text{FeOOH}$  was grown on FTO by the same hydrothermal process but further treated in a tubular furnace at different air pressures.  $\text{FeOOH}$  was firstly sintered at  $550^\circ\text{C}$  for 2 h in a relatively high vacuum environment (1 Pa), and then annealed at  $750^\circ\text{C}$  for 15 min in a relatively low vacuum environment (optimized to 2500 Pa) (Fig. 1a). The final sample treated in the low vacuum environment was labeled as  $\text{Fe}_2\text{O}_3$  (LV). The pressure for annealing process at  $750^\circ\text{C}$  for 15 min was also optimized from 1 Pa to 1 atm, and the sample treated at a relatively high vacuum of 1 Pa was labeled as  $\text{Fe}_2\text{O}_3$  (HV). The annealing temperature was also optimized from  $550^\circ\text{C}$  to  $760^\circ\text{C}$ .

### 2.4. Synthesis of $\text{Hf-Fe}_2\text{O}_3$ , $\text{Hf-Fe}_2\text{O}_3$ (LV), $\text{P-Hf-Fe}_2\text{O}_3$ (LV) and $\text{FeNiOOH-P-Hf-Fe}_2\text{O}_3$ (LV)

Hf-modified  $\text{Fe}_2\text{O}_3$  photoanodes were prepared by similar processes except for adding hafnium chloride as the Hf precursor in the initial hydrothermal process.  $100 \mu\text{l}$  nitric acid was also added into the initial solution to control the pH value. P-modified  $\text{Fe}_2\text{O}_3$  photoanodes were prepared by simply immersing the photoanodes in phosphoric acid solution with different concentrations (labeled as  $\text{P-Hf-Fe}_2\text{O}_3$  (LV)). The deposition of  $\text{FeNiOOH}$  co-catalyst followed the photo-assisted

electrodeposition method reported in the literature (labeled as  $\text{FeNiOOH-P-Hf-Fe}_2\text{O}_3$  (LV)) [30].

### 2.5. Structural characterization

Scanning Electron Microscope (SEM, FEI Quanta 200 F), X-ray photoelectron Spectrometer (XPS, Kratos AXIS UltraDLD), High-Resolution Transmission Electron Microscopy (HRTEM, FEI Tecnai G2 F20 S-TIWN), and X-ray Diffraction (XRD, PANalytical, Zmpyrean) were used for structural characterization. X-ray absorption spectroscopy (XAS) experiments were conducted at the Shanghai Synchrotron Radiation Facility (SSRF, 11B) and the National Synchrotron Radiation Laboratory (NSRL, Beamlines MCD-A and MCD-B (Soochow Beamline for Energy Materials)).

### 2.6. Electrochemical measurement

The PEC measurement was conducted using an electrochemical workstation (CHI 660D) with a three-electrode PEC cell at room temperature ( $\sim 25^\circ\text{C}$ ) [4,30]. The working area was about  $0.1 \text{ cm}^2$  and the work area is surrounded by non-conductive, light-tight black insulating tape. Xenon High Brightness Cold Light Source (XD-300) was coupled with AM 1.5 G filter, which was used as the light source and the power density was set to  $100 \text{ mW cm}^{-2}$ . For transient photo-induced voltage (TPV) measurements, the samples were excited by a laser radiation pulse (wavelength 355 nm, pulse width 5 ns) from a third-harmonic Nd:YAG laser (Polaris II, New Wave Research, Inc.). The product gases of  $\text{H}_2$  and  $\text{O}_2$  were measured by a gas chromatograph (GC-7900, Techcomp, Shanghai, China).

### 2.7. Tandem system for solar water splitting

A commercial Si solar cell has been directly connected to the hematite photoanode to form a tandem system. The solar cell has a short-circuit current ( $J_{sc}$ ) of  $7.665 \text{ mA/cm}^2$ , an open-circuit voltage ( $V_{oc}$ ) of  $1.276 \text{ V}$ , and a fill factor (FF) of 75.14%. The power conversion efficiency (PCE) of the solar cell is 7.35%. The system has been illuminated by Xenon High Brightness Cold Light Sources (XD-300) coupled with AM 1.5 G filter ( $100 \text{ mW cm}^{-2}$ ). The illumination area for hematite is  $0.5 \text{ cm}^2$  while it is  $0.2 \text{ cm}^2$  for the solar cell. STH efficiency is defined as the "chemical energy produced" divided by the "solar energy input". The chemical energy produced can be expressed as the rate of hydrogen production ( $11.4 \times 10^{-6} \text{ mmol H}_2/\text{s}$ ) multiplied by the change in Gibbs free energy per mol of  $\text{H}_2$  ( $\Delta G = 2.37 \times 10^5 \text{ J mol}^{-1}$  at  $25^\circ\text{C}$ ). The total solar energy input can be the sum of incident light on hematite ( $100 \times 0.5 \text{ mW}$ ) and incident light on solar cell after conversion ( $100 \times 0.2 \times 7.35\% \text{ mW}$ ). Then the calculated STH for the tandem system is 5.3%.

## 3. Results and discussion

### 3.1. Morphology and structure characterization

The pristine  $\text{Fe}_2\text{O}_3$  photoanode was prepared by a modified hydrothermal method [4,16,29,30]. The hematite photoanodes with oxygen vacancy and  $\beta\text{-Fe}_2\text{O}_3$  were prepared at different pressure and temperature. The optimized sample treated in a low vacuum and a high temperature was labeled as  $\text{Fe}_2\text{O}_3$  (LV). The synthesis processes are described in Fig. 1a. The SEM, TEM and HRTEM images of  $\text{Fe}_2\text{O}_3$  and  $\text{Fe}_2\text{O}_3$  (LV) are shown in Fig. 1b and c, respectively. From the SEM images, uniform hematite nanorods on FTO can be observed in both samples. The cross-section images are shown in Fig. S1, suggesting a thickness about 250 nm. Fig. S1a also shows the corresponding XRD pattern, which reveals the successful preparation of hematite crystal structure on FTO in both pristine  $\text{Fe}_2\text{O}_3$  and  $\text{Fe}_2\text{O}_3$  (LV) [4]. From the TEM images, the pristine  $\text{Fe}_2\text{O}_3$  shows a solid nanorod morphology,



while the  $\text{Fe}_2\text{O}_3$  (LV) sample treated in a low vacuum and a high temperature exhibits a porous nanorod structure. The porous structure is favorable for the charge transfer with a shorter distance to the surface, which also shows more electrochemical surface areas (ECSAs) as measured in 1 M NaOH ( $0.0988 \text{ mF cm}^{-2}$  for  $\text{Fe}_2\text{O}_3$  (LV) while  $0.0343 \text{ mF cm}^{-2}$  for  $\text{Fe}_2\text{O}_3$ ). The elemental mappings of  $\text{Fe}_2\text{O}_3$  (LV) in Fig. 1d-f also reveal the existence of Fe and O in hematite with the diffusion of Sn (tin) from FTO [16]. Similar mapping results for the pristine  $\text{Fe}_2\text{O}_3$  are shown in Fig. S2.

HRTEM images (Fig. 1b-3 and c-3) are also shown to clearly identify the microstructure. The pristine  $\text{Fe}_2\text{O}_3$  shows clear and continuous hematite crystal lattice. Interestingly, except for the typical hematite lattice, the  $\text{Fe}_2\text{O}_3$  (LV) sample also exhibits many hetero crystal structures (labeled as dash line), as shown in Fig. 1c-3. More HRTEM images for  $\text{Fe}_2\text{O}_3$  (LV) can be found in Fig. 2a and c, which show clear  $\beta\text{-Fe}_2\text{O}_3$  lattice structure. To verify the presence of  $\beta\text{-Fe}_2\text{O}_3$  in  $\text{Fe}_2\text{O}_3$  (LV), XRD data for  $\text{Fe}_2\text{O}_3$  and  $\text{Fe}_2\text{O}_3$  (LV) are carefully analyzed as shown in Fig. 2b. After the low vacuum and high temperature treatment, some new XRD peaks (around  $24^\circ$  and  $33^\circ$ ) are observed in  $\text{Fe}_2\text{O}_3$  (LV), which can be attributed to the formation of  $\beta\text{-Fe}_2\text{O}_3$  (PDF#39-0238 and PDF#76-1821) [27]. The introduction of small hetero structures in the bulk of hematite has created abundant interfacial structures, which might be favorable for the catalytic performance [28].

The low vacuum treatment can also introduce oxygen vacancies in hematite [18]. XPS spectra of  $\text{Fe}_2\text{O}_3$  and  $\text{Fe}_2\text{O}_3$  (LV) are used to probe the electronic structure changes. The XPS survey scans of  $\text{Fe}_2\text{O}_3$  and  $\text{Fe}_2\text{O}_3$  (LV) are shown in Fig. S3a. Both samples show clear Fe and O signals for the formation of  $\text{Fe}_2\text{O}_3$  [4,31]. Sn signal in Fig. S3a can be attributed to the Sn diffusion from FTO substrate, while C signal comes from the contaminations [4,16]. It is well known that Sn diffusion in hematite can increase the carrier density and then improve the electrical

conductivity, leading to enhanced photocurrent [16,32]. The Sn signal in  $\text{Fe}_2\text{O}_3$  (LV) is more prominent than that in  $\text{Fe}_2\text{O}_3$ , which may partly contribute to an enhanced performance. Fig. 2d shows the high resolution XPS spectra at Fe 2p and an obvious feature for  $\text{Fe}^{2+}$  (around 716 eV) can be observed in  $\text{Fe}_2\text{O}_3$  (LV), strongly suggesting the presence of oxygen vacancies in  $\text{Fe}_2\text{O}_3$  (LV) [18,31,33].

The electronic structure changes have been further probed by synchrotron radiation based X-ray absorption spectroscopy (XAS). The normalized O K-edge XAS spectra of  $\text{Fe}_2\text{O}_3$  and  $\text{Fe}_2\text{O}_3$  (LV) are shown in Fig. S3b. Two separated pre-peaks (A1 and A2) around 530 eV can be observed, which are attributed to the transitions from O (1s) to the hybridized O(2p)-Fe(3d) state [34,35]. The main broad feature B (around 540 eV) can be attributed to the hybridization of O 2p and Fe 4sp states [35–38]. Compared to pristine  $\text{Fe}_2\text{O}_3$ , the O K-edge spectrum of  $\text{Fe}_2\text{O}_3$  (LV) shows a reduced intensity of the pre-peaks (A1 and A2) and an increased feature B. The decreased pre-peaks can be attributed to the formation of reduced Fe (such as  $\text{Fe}^0$  or  $\text{Fe}^{2+}$ ) according to the literature [23,39,40], confirming the creation of oxygen vacancies in  $\text{Fe}_2\text{O}_3$  (LV). The increased feature B can be attributed to the increased Sn in  $\text{Fe}_2\text{O}_3$  (LV) with more oxygen vacancies [41]. Fe K-edge XAS spectra in hard X-ray range are measured to further probe the bulk information, as shown in Fig. S4a. The XAS spectrum of  $\text{Fe}_2\text{O}_3$  (LV) is almost identical to that of  $\text{Fe}_2\text{O}_3$ . However, the corresponding Fourier transform curves for  $\text{Fe}_2\text{O}_3$  and  $\text{Fe}_2\text{O}_3$  (LV) in Fig. 2e (or Fig. S4) show clear difference. The peak intensities for  $\text{Fe}_2\text{O}_3$  (LV) are obviously lower than that for  $\text{Fe}_2\text{O}_3$  in Fig. 2e. The lower Fe-O peak intensity suggests the reduced Fe-O bonds with oxygen vacancies. The lower Fe-Fe peak intensity indicates decreased coordination number, which originates from the formation of oxygen vacancies or interfacial structures around the hetero phases. The XAS spectrum and the EXAFS data of  $\text{Fe}_2\text{O}_3$  (HV) treated in a high vacuum are also provided in Fig. S4, where the EXAFS peak intensities further decrease with more oxygen vacancies or interfacial

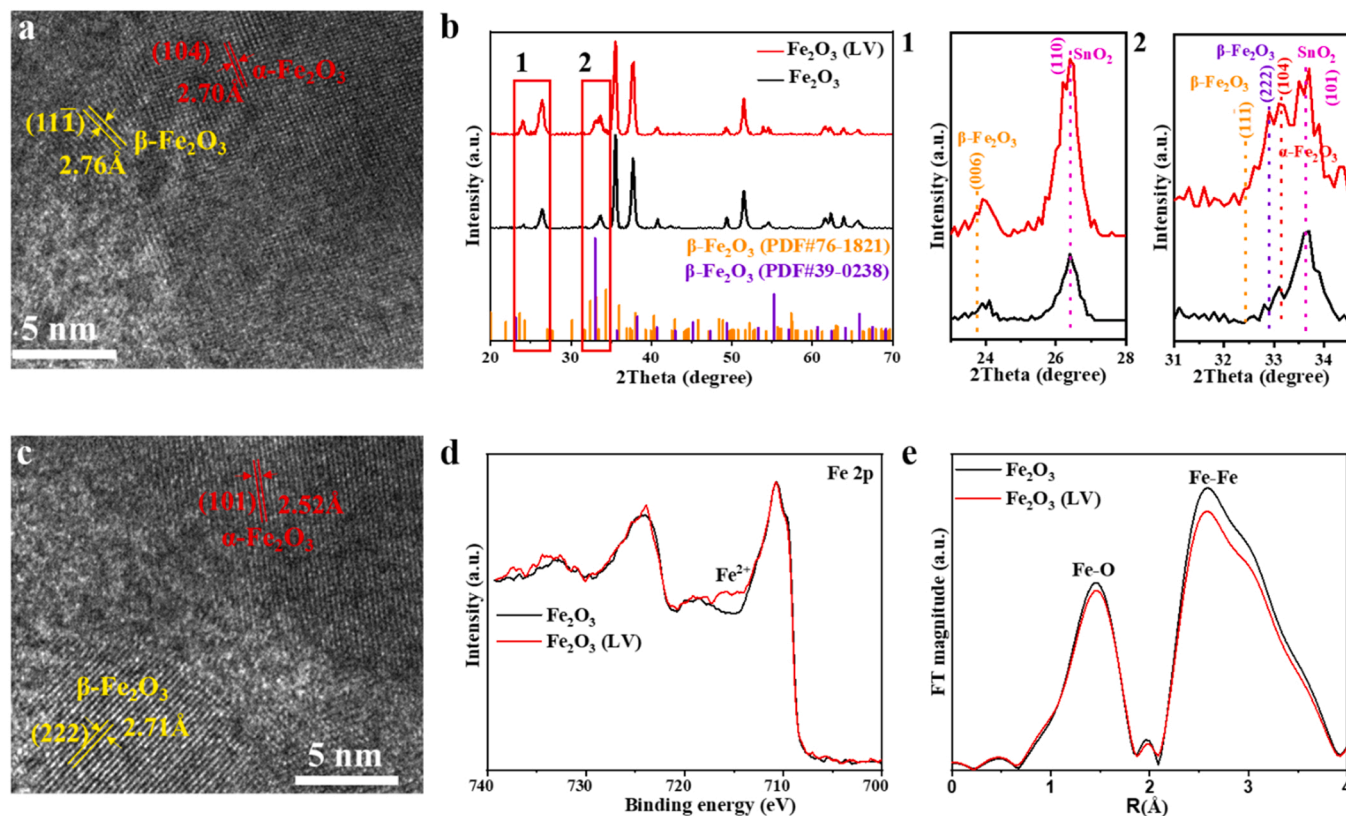


**Fig. 2.** The structure analysis of various photoanodes. (a,c) HRTEM images of  $\text{Fe}_2\text{O}_3$  (LV). (b) XRD spectra of  $\text{Fe}_2\text{O}_3$  and  $\text{Fe}_2\text{O}_3$  (LV) with the reference data of  $\beta\text{-Fe}_2\text{O}_3$ . (d) High-resolution Fe 2p spectra of  $\text{Fe}_2\text{O}_3$  and  $\text{Fe}_2\text{O}_3$  (LV). (e) Fourier transform curves of the Fe K-edge EXAFS data of  $\text{Fe}_2\text{O}_3$  and  $\text{Fe}_2\text{O}_3$  (LV).



structures. The results strongly confirm that oxygen vacancies have been successfully created in  $\text{Fe}_2\text{O}_3$  (LV).

### 3.2. Photoelectrochemical activity and mechanism

Fig. 3a shows the PEC performance of  $\text{Fe}_2\text{O}_3$ , and  $\text{Fe}_2\text{O}_3$  (LV). The performance for  $\text{Fe}_2\text{O}_3$  (LV) treated at  $700^\circ\text{C}$  (labeled as  $\text{Fe}_2\text{O}_3$  (LV 700)) is also shown for comparison. The pristine  $\text{Fe}_2\text{O}_3$  shows a photocurrent of  $0.82\text{ mA/cm}^2$  at  $1.23\text{ V}$  (vs. RHE), in good agreement with the literature [4,20]. Interestingly,  $\text{Fe}_2\text{O}_3$  (LV) can reach a high photocurrent of  $2.72\text{ mA/cm}^2$  at  $1.23\text{ V}$  vs. RHE, which is 3.3 times of that for the pristine  $\text{Fe}_2\text{O}_3$ . To understand the effects of pressure and temperature,  $J$ - $V$  curves and XRD spectra at different pressures and temperatures have been measured and shown in Fig. 4. At a low pressure of  $1\text{ Pa}$  with deficient oxygen (at  $750^\circ\text{C}$ ), the sample shows a very low performance in Fig. 4a. The corresponding XRD spectrum shows a peak around  $30^\circ$ , indicating the formation of  $\text{Fe}_3\text{O}_4$  which is inactive for PEC reaction. At a high pressure of  $1\text{ atm}$ , the  $J$ - $V$  curve is similar to that for the pristine hematite without oxygen vacancies. Thus, a suitable oxygen vacancy content in hematite, such as that at the pressure of  $2500\text{ Pa}$ , is a key issue to obtain the high PEC performance. The reaction temperature is also investigated. Interestingly, even at a high temperature of  $700^\circ\text{C}$ , the photocurrent is still around  $1.63\text{ mA/cm}^2$  at  $1.23\text{ V}$  vs. RHE, while it sharply increases to  $2.72\text{ mA/cm}^2$  at  $750^\circ\text{C}$ . The photocurrent at a relatively low temperature of  $700^\circ\text{C}$  is similar to the normally obtained value of  $1.82\text{ mA/cm}^2$  reported in the literature with oxygen vacancy [18], while the great enhancement to  $2.72\text{ mA/cm}^2$  at  $750^\circ\text{C}$  should be attributed to different reason. The corresponding XRD spectra are thus shown in Fig. 4d to understand the effect. Interestingly, obvious peaks for  $\beta\text{-Fe}_2\text{O}_3$  can be observed in the XRD spectrum at  $750^\circ\text{C}$ , while they cannot be clearly observed in the spectra treated at even  $700^\circ\text{C}$  or lower. The results strongly suggest that the significant photocurrent enhancement should be attributed to the formation of  $\beta\text{-Fe}_2\text{O}_3$  in

hematite. Thus, the pressure mainly tunes the oxygen vacancy content while the temperature mainly contributes to the formation of  $\beta\text{-Fe}_2\text{O}_3$ . The high PEC performance only occurs in the sample with both the hetero phase of  $\beta\text{-Fe}_2\text{O}_3$  and suitable oxygen vacancies as shown in Fig. 4, confirming their synergistic effect to simultaneously enhance the PEC performance.

The PEC curves of  $\text{Fe}_2\text{O}_3$ ,  $\text{Fe}_2\text{O}_3$  (LV) (at  $750^\circ\text{C}$ ) and  $\text{Fe}_2\text{O}_3$  (LV 700) are clearly compared in Fig. 3a. The  $\text{Fe}_2\text{O}_3$  (LV 700) sample with optimized pressure shows an enhanced photocurrent when compared to that of  $\text{Fe}_2\text{O}_3$ , due to the effect of oxygen vacancy. However, a higher onset potential can also be observed due to the formation of defects along with oxygen vacancy, similar to the literature [19,21]. Interestingly,  $\text{Fe}_2\text{O}_3$  (LV) with  $\beta\text{-Fe}_2\text{O}_3$  not only shows a further increased photocurrent, but also exhibits a significantly lowered onset potential (around  $100\text{ mV}$ ) when compared to that of  $\text{Fe}_2\text{O}_3$  (LV 700), strongly suggesting the positive effect of  $\beta\text{-Fe}_2\text{O}_3$  for enhanced performance.

The working mechanism of oxygen vacancy and  $\beta\text{-Fe}_2\text{O}_3$  in hematite has been probed. Previous work had shown that oxygen vacancy in hematite could enhance the PEC performance by improving the charge transport [18–20]. Mott-Schottky plots of  $\text{Fe}_2\text{O}_3$ ,  $\text{Fe}_2\text{O}_3$  (LV) and  $\text{Fe}_2\text{O}_3$  (LV 700) are thus shown in Fig. 3b. The slopes in Fig. 3b can be used to calculate the carrier densities, which are  $6.41 \times 10^{19}\text{ cm}^{-3}$ ,  $7.53 \times 10^{20}\text{ cm}^{-3}$ , and  $6.01 \times 10^{20}\text{ cm}^{-3}$  for  $\text{Fe}_2\text{O}_3$ ,  $\text{Fe}_2\text{O}_3$  (LV) and  $\text{Fe}_2\text{O}_3$  (LV 700), respectively. Compared to the pristine  $\text{Fe}_2\text{O}_3$ , the carrier density in  $\text{Fe}_2\text{O}_3$  (LV 700) has been significantly enhanced by around one order with the presence of oxygen vacancy. However, with the further creation of  $\beta\text{-Fe}_2\text{O}_3$ , the carrier density in  $\text{Fe}_2\text{O}_3$  (LV) only slightly increases, suggesting a weak contribution from hetero phase to the carrier density. The increased carrier density is mainly from oxygen vacancy, which will improve the electrical conductivity for better charge transfer and then facilitate the collection efficiency of photo-excited electrons [18].

The charge separation efficiencies are also probed to understand the working mechanism.  $J$ - $V$  curves measured with and without  $\text{H}_2\text{O}_2$

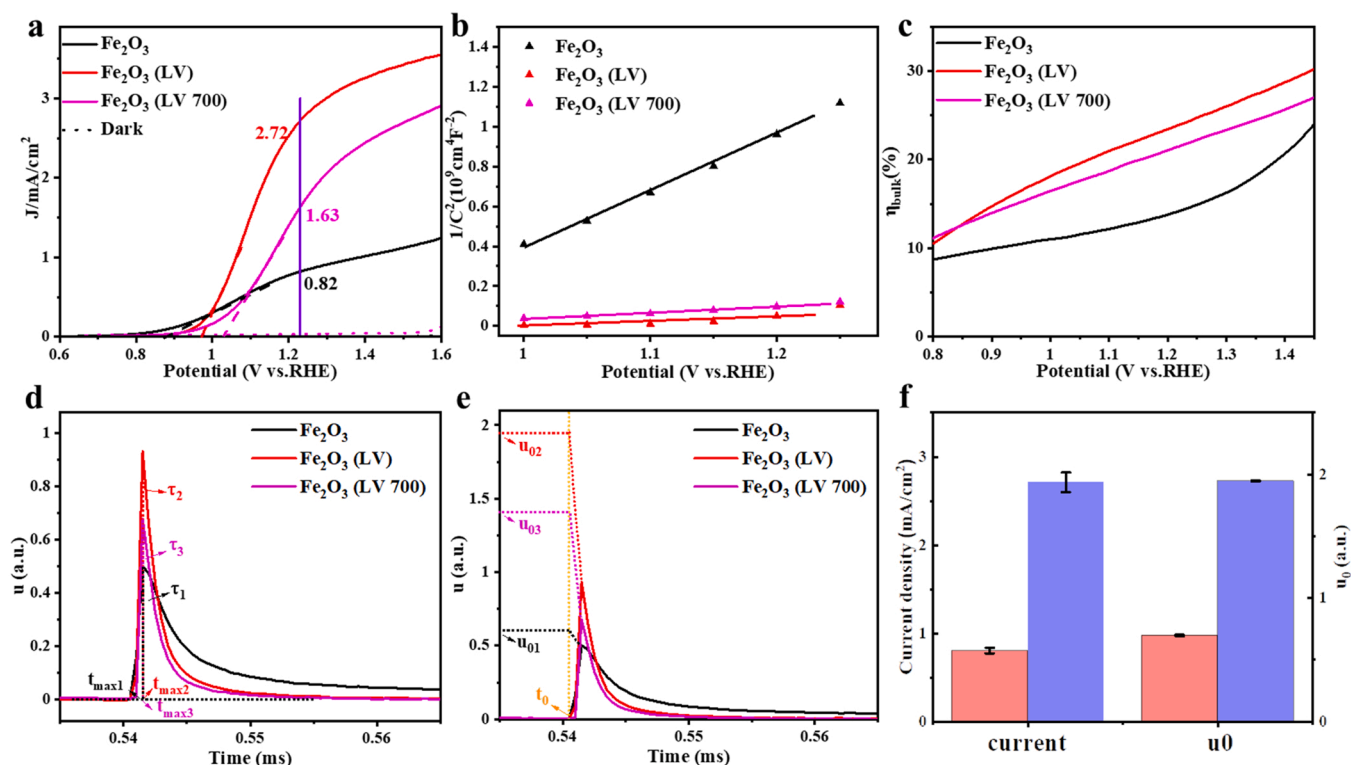


**Fig. 3.** Electrochemical analysis of  $\text{Fe}_2\text{O}_3$  (LV). (a,b)  $J$ - $V$  curves (a) and Mott-Schottky plots (b) of  $\text{Fe}_2\text{O}_3$ ,  $\text{Fe}_2\text{O}_3$  (LV) and  $\text{Fe}_2\text{O}_3$  (LV 700). (c) Bulk charge separation efficiencies ( $\eta_{\text{bulk}}$ ) of  $\text{Fe}_2\text{O}_3$ ,  $\text{Fe}_2\text{O}_3$  (LV) and  $\text{Fe}_2\text{O}_3$  (LV 700). (d) TPV relaxation curves and charge extraction rates ( $t_{\text{max}}$ ) of  $\text{Fe}_2\text{O}_3$ ,  $\text{Fe}_2\text{O}_3$  (LV) and  $\text{Fe}_2\text{O}_3$  (LV 700). (e) The corresponding extrapolation ( $u_0$ ) values of TPV curves. (f) Comparison of the photocurrent density ( $1.23\text{ V}$  vs. RHE) and  $u_0$  of  $\text{Fe}_2\text{O}_3$  and  $\text{Fe}_2\text{O}_3$  (LV).

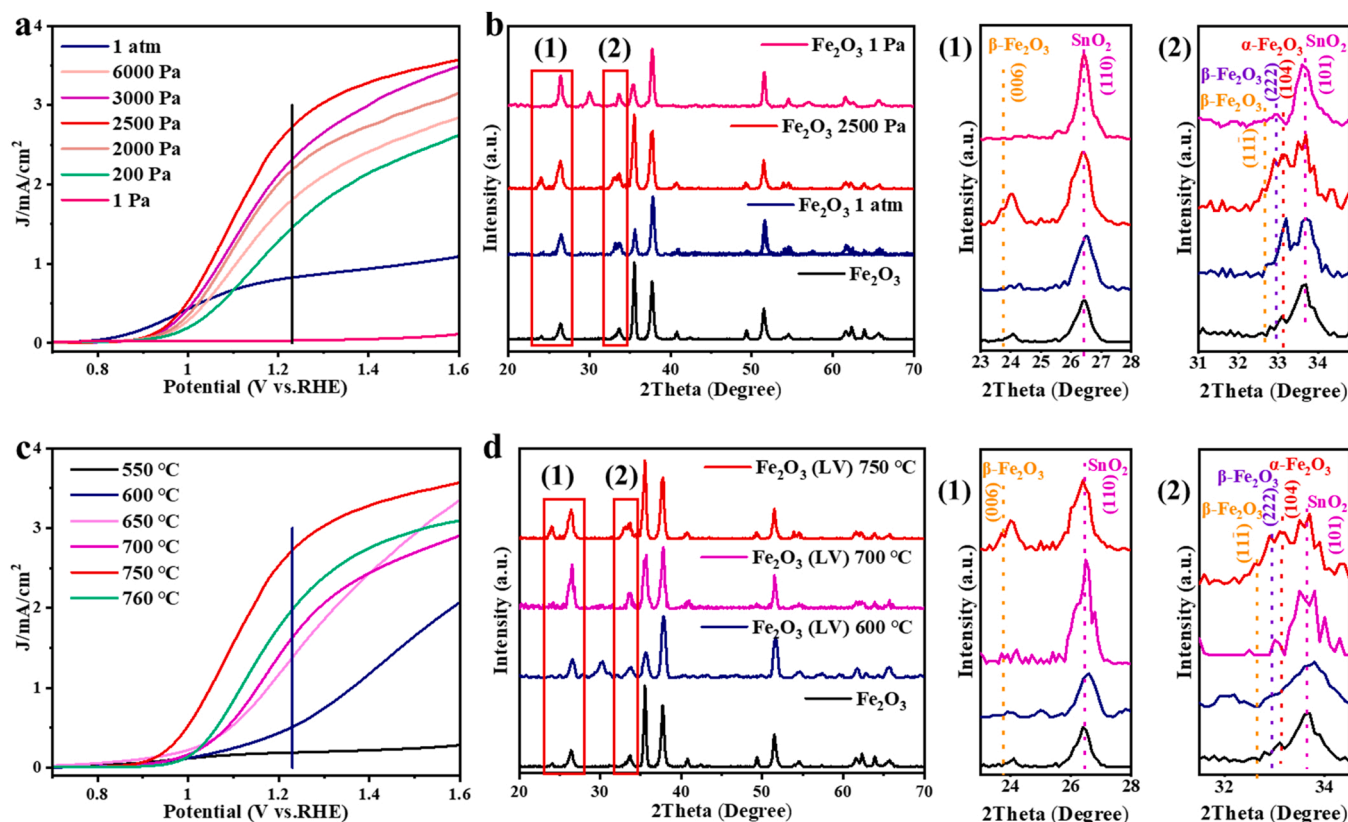


**Fig. 4.** Optimization of pressure and temperature. (a,b) *J-V* curves (a) and XRD spectra (b) of the Fe<sub>2</sub>O<sub>3</sub> samples treated at different pressures (1 Pa to 1 atm). (c,d) *J-V* curves (c) and XRD spectra (d) of the Fe<sub>2</sub>O<sub>3</sub> samples treated at different temperatures (550–760 °C) for 15 min.

(0.5 M) as the sacrificial agent have been shown in Fig. S5a, b, and c for Fe<sub>2</sub>O<sub>3</sub>, Fe<sub>2</sub>O<sub>3</sub> (LV) and Fe<sub>2</sub>O<sub>3</sub> (LV 700), respectively [4,15]. The curve with H<sub>2</sub>O<sub>2</sub> can be considered to show 100% efficiency and the surface charge separation efficiency  $\eta_{surf}$  can be calculated by the formula:  $\eta_{surf} = J_{H_2O_2}/J_{H_2O_2}$  ( $J$  is photocurrent density) [15]. The bulk charge separation efficiency ( $\eta_{bulk}$ ) can be calculated by the formula:  $\eta_{bulk} = J_{H_2O_2}/J_{abs}$  [4].  $J_{abs}$  can be calculated according to the following equation:  $J_{abs}(\lambda) = \int N_{ph}(\lambda) \cdot LHE(\lambda) \cdot e d\lambda$  (where  $\lambda$  is the wavelength (nm),  $N_{ph}(\lambda)$  is the photon flux (mW cm<sup>-2</sup> nm<sup>-1</sup>),  $e$  is the elementary charge ( $e = 1.602 \times 10^{-19}$ ),  $LHE(\lambda)$  is the light harvesting efficiency) [42].

Fig. 3c shows the bulk charge separation efficiencies of Fe<sub>2</sub>O<sub>3</sub>, Fe<sub>2</sub>O<sub>3</sub> (LV) and Fe<sub>2</sub>O<sub>3</sub> (LV 700). It can be observed that in the whole potential range Fe<sub>2</sub>O<sub>3</sub> (LV 700) exhibits an enhanced bulk charge separation efficiency than that of Fe<sub>2</sub>O<sub>3</sub>, due to the improved electrical conductivity. Interestingly, Fe<sub>2</sub>O<sub>3</sub> (LV) with β-Fe<sub>2</sub>O<sub>3</sub> can further enhance the bulk charge separation efficiency. Especially, the  $\eta_{bulk}$  value at 1.23 V vs. RHE is only 14.4% for Fe<sub>2</sub>O<sub>3</sub>, and 21.7% for Fe<sub>2</sub>O<sub>3</sub> (LV 700), while it is 24.2% for Fe<sub>2</sub>O<sub>3</sub> (LV). The increased bulk charge separation efficiency can be attributed to the presence of β-Fe<sub>2</sub>O<sub>3</sub>. The surface charge separation efficiencies are also compared in Fig. S5d. Fe<sub>2</sub>O<sub>3</sub> (LV 700) shows better surface charge separation efficiencies than Fe<sub>2</sub>O<sub>3</sub> after 1.17 V vs. RHE, while Fe<sub>2</sub>O<sub>3</sub> (LV) exhibits greatly enhanced efficiencies than Fe<sub>2</sub>O<sub>3</sub> (LV 700) after 0.95 V vs. RHE. Especially, the  $\eta_{surf}$  value at 1.23 V vs. RHE is 42.3% for Fe<sub>2</sub>O<sub>3</sub>, and 55.6% for Fe<sub>2</sub>O<sub>3</sub> (LV 700), while it can be significantly improved to 83.9% for Fe<sub>2</sub>O<sub>3</sub> (LV). The enhancement is also consistent with the *J-V* curve which shows an obvious onset potential shift.

The significant enhancement of both bulk and surface charge separation efficiencies in Fe<sub>2</sub>O<sub>3</sub> (LV) suggests that the formation of β-Fe<sub>2</sub>O<sub>3</sub> can effectively modulate the bulk charge utilization in hematite by a unique way. Fig. 3b has revealed that the increased carrier density is not

from β-Fe<sub>2</sub>O<sub>3</sub>. β-Fe<sub>2</sub>O<sub>3</sub> itself is also not an active material for solar water splitting [27]. However, the creation process of β-Fe<sub>2</sub>O<sub>3</sub> will lead to abundant interfacial structures [28], as also observed in Fig. 2a and c. The interfacial structures contain many disordered components, which are favourable for the formation of oxygen vacancies due to the relatively low formation energy [22,43]. With the presence of many oxygen vacancies in the interfacial regions, the disordered structures may reduce the bulk (and/or near surface) defects. Actually, the abundant oxygen vacancies created in the interfacial region were already reported in the literature to improve the PEC performance [22,44]. Thus the formation of β-Fe<sub>2</sub>O<sub>3</sub> itself will not improve the PEC performance of hematite, while the corresponding interfacial structures can optimize the internal structure of hematite and then reduce the defects. The bulk and surface charge separation efficiencies can thus be further improved, with less electron-hole recombination. As a result, the onset potential can be significantly lowered and the photocurrent can be increased in the Fe<sub>2</sub>O<sub>3</sub> (LV) sample. The combination of oxygen vacancy and hetero phase can synergistically work to improve the PEC performance by both increasing the charge transport and reducing the defects, leading to suppressed charge recombination for enhanced PEC performance. It should be noted that although the defects have been significantly reduced by hetero phase in hematite, the defects at the solid-liquid interface can still exist [45], resulting in the lower surface charge separation efficiency of Fe<sub>2</sub>O<sub>3</sub> (LV) than that of Fe<sub>2</sub>O<sub>3</sub> before 1.1 V vs. RHE in Fig. S5d. The UV-Vis absorption spectra of Fe<sub>2</sub>O<sub>3</sub>, Fe<sub>2</sub>O<sub>3</sub> (LV), and Fe<sub>2</sub>O<sub>3</sub> (LV 700) are also shown in Fig. S5e, where no obvious difference can be observed. Fig. S5f also shows the IPCE values (lower left) and the stability curve (upper right). Fe<sub>2</sub>O<sub>3</sub> (LV) photoanode exhibits much higher IPCE values than that of Fe<sub>2</sub>O<sub>3</sub> in the whole range, in good agreement with the PEC performance. The Fe<sub>2</sub>O<sub>3</sub> (LV) photoanode is also stable as shown in Fig. S5f.

Furthermore, transient photo-induced voltage (TPV) measurements

were used to explore the interfacial charge transfer kinetics of  $\text{Fe}_2\text{O}_3$ ,  $\text{Fe}_2\text{O}_3$  (LV) and  $\text{Fe}_2\text{O}_3$  (LV 700) [46,47]. The TPV curves have been excited by a laser (355 nm) and the laser-induced electrons can be collected from the conductive FTO substrate, as noted by TPV curves [46,47]. A higher TPV curve intensity stands for more electrons excited by the laser. It is a model by using laser but similar effect can be extended to the sunlight with a broad wavelength range, in which higher TPV curve intensity suggests better charge extraction efficiency to produce more electron-hole pairs under the same illumination [46,47]. Fig. 3d exhibits the TPV relaxation curves of  $\text{Fe}_2\text{O}_3$ ,  $\text{Fe}_2\text{O}_3$  (LV) and  $\text{Fe}_2\text{O}_3$  (LV 700), in which the photovoltage intensity of  $\text{Fe}_2\text{O}_3$  (LV) is much higher than that of  $\text{Fe}_2\text{O}_3$  and  $\text{Fe}_2\text{O}_3$  (LV 700), suggesting more excited electrons from  $\text{Fe}_2\text{O}_3$  (LV) in the PEC process (better charge extraction efficiency). The charge extraction rate of  $\text{Fe}_2\text{O}_3$  (LV) ( $t_{\text{max}2}$ ) is slightly larger than that of  $\text{Fe}_2\text{O}_3$  ( $t_{\text{max}1}$ ). When the TPV curve is extrapolated to  $t = t_0$  in Fig. 3e, the corresponding intensity of  $u_0$  can also be obtained, which can be used to estimate the number of electrons which will be excited by the sunlight in the photoanode [46,47]. The intensity of  $u_0$  for  $\text{Fe}_2\text{O}_3$  (LV) is also much higher than that for  $\text{Fe}_2\text{O}_3$  and  $\text{Fe}_2\text{O}_3$  (LV 700), suggesting more potential electron-hole pairs which can be excited in  $\text{Fe}_2\text{O}_3$  (LV). Thus, the presence of oxygen vacancy and  $\beta\text{-Fe}_2\text{O}_3$  can effectively increase the charge extraction capability in

hematite to create more photo-generated electron-hole pairs. Fig. 3f also shows a comparison of the photocurrent density (at 1.23 V vs. RHE) and  $u_0$  for  $\text{Fe}_2\text{O}_3$  and  $\text{Fe}_2\text{O}_3$  (LV). Interestingly, the  $u_0$  value for  $\text{Fe}_2\text{O}_3$  (LV) is 2.79 times to that for  $\text{Fe}_2\text{O}_3$ , similar to the current density ratio for  $\text{Fe}_2\text{O}_3$  (LV) and  $\text{Fe}_2\text{O}_3$  (3.3). The similar ratios suggest that the enhanced charge extraction capability ( $u_0$ ) can be effectively used and the increased photo-generated holes can be quickly transferred to the surface for OER. With the enhanced extraction and separation (see Fig. 3c) efficiencies of photo-generated charge, the PEC performance of  $\text{Fe}_2\text{O}_3$  (LV) with oxygen vacancy and  $\beta\text{-Fe}_2\text{O}_3$  can thus be significantly improved, as shown in Fig. 3a.

$\text{Fe}_2\text{O}_3$  (LV) with oxygen vacancy and  $\beta\text{-Fe}_2\text{O}_3$  shows an excellent PEC performance. Since the introduction of oxygen vacancy and  $\beta\text{-Fe}_2\text{O}_3$  is an intrinsic modification without significant structure changes, the  $\text{Fe}_2\text{O}_3$  (LV) sample can thus be used as a good starting material to couple with various modifications. For example,  $\text{Fe}_2\text{O}_3$  (LV) mainly improve the bulk charge utilization but the surface defects may also increase (Fig. S5d), which needs to be fixed by surface modifications. Phosphorus (P) based surface treatments were widely reported to modify the surface property of hematite for enhanced PEC performance [48–51]. Especially, P-treatment can form a gradient electric field to improve the surface hole transfer and then facilitate the surface water oxidation [50].

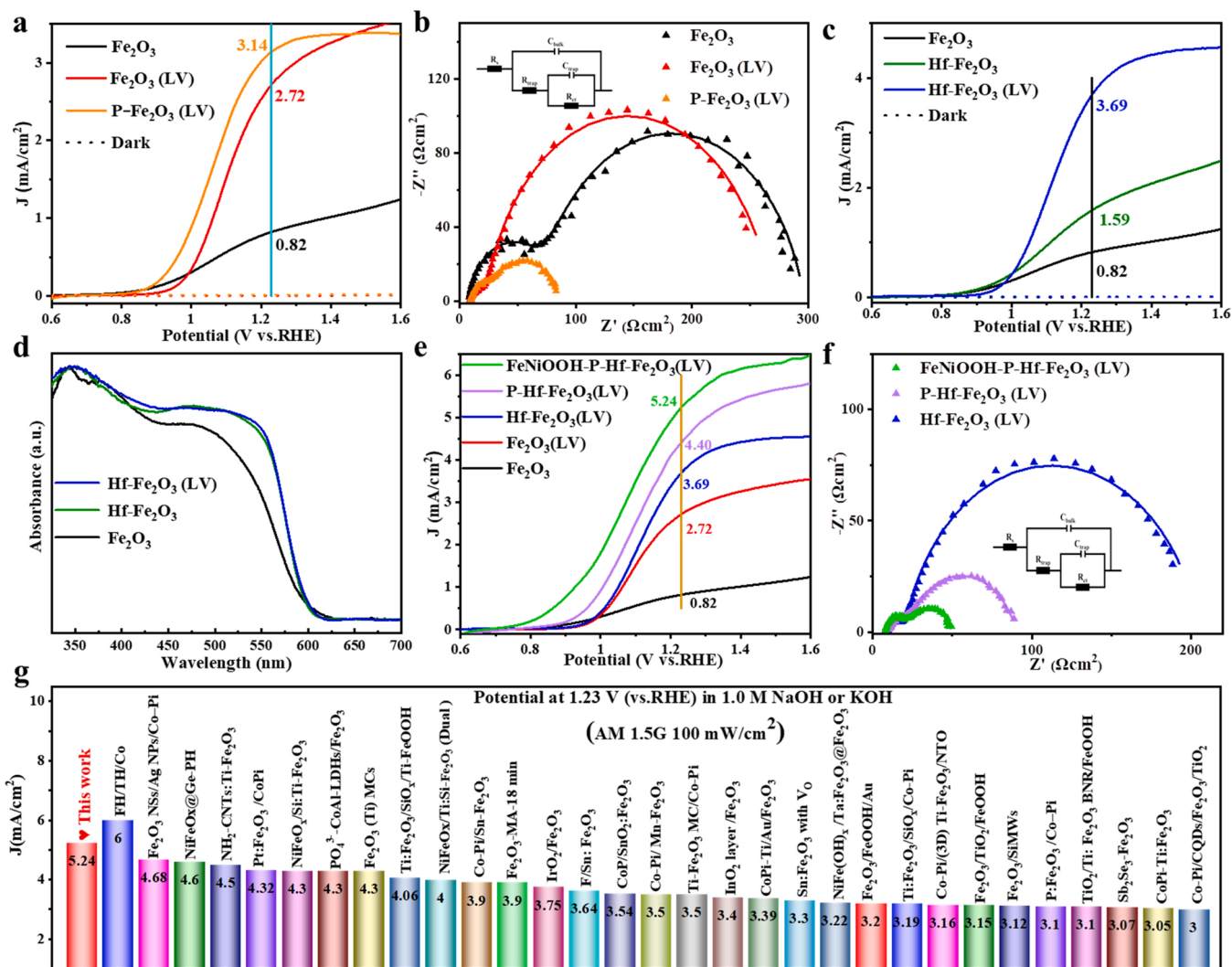


**Fig. 5.** PEC performances of  $\text{P-Fe}_2\text{O}_3$  (LV),  $\text{Hf-Fe}_2\text{O}_3$  (LV) and  $\text{FeNiOOH-P-Hf-Fe}_2\text{O}_3$  (LV). (a,b)  $J$ -V curves (a) and EIS spectra (b) of  $\text{Fe}_2\text{O}_3$ ,  $\text{Fe}_2\text{O}_3$  (LV) and  $\text{P-Fe}_2\text{O}_3$  (LV). (c,d)  $J$ -V curves (c) and UV-visible absorption spectra (d) of  $\text{Fe}_2\text{O}_3$ ,  $\text{Hf-Fe}_2\text{O}_3$  and  $\text{Hf-Fe}_2\text{O}_3$  (LV). (e)  $J$ -V curves of  $\text{Fe}_2\text{O}_3$ ,  $\text{Fe}_2\text{O}_3$  (LV),  $\text{Hf-Fe}_2\text{O}_3$  (LV),  $\text{P-Hf-Fe}_2\text{O}_3$  (LV) and  $\text{FeNiOOH-P-Hf-Fe}_2\text{O}_3$  (LV). (f) EIS spectra of  $\text{Hf-Fe}_2\text{O}_3$  (LV),  $\text{P-Hf-Fe}_2\text{O}_3$  (LV) and  $\text{FeNiOOH-P-Hf-Fe}_2\text{O}_3$  (LV). (g) Comparison of the PEC performance on hematite-based photoanodes (at 1.23 V vs. RHE).



Here we modify the  $\text{Fe}_2\text{O}_3$  (LV) sample by a simple P-treatment (see experimental details). Fig. S6a and b show the XPS and XAS spectra of P- $\text{Fe}_2\text{O}_3$  (LV), respectively. Both the XPS (around 134 eV) and XAS peaks (around 138 eV and 147 eV) are in good agreement with that for  $\text{FePO}_4$  in the literature [50,51], suggesting the successful P-treatment in P- $\text{Fe}_2\text{O}_3$  (LV). Due to the accelerated surface charge transfer by P-treatment [48–51], the photocurrent of P- $\text{Fe}_2\text{O}_3$  (LV) at 1.23 V vs. RHE can be enhanced from 2.72  $\text{mA}/\text{cm}^2$  to 3.14  $\text{mA}/\text{cm}^2$  as shown in Fig. 5a. Moreover, the onset potential of P- $\text{Fe}_2\text{O}_3$  (LV) shows an obvious cathodic shift, confirming the modified surface property. The surface charge transfer is also probed by the electrochemical impedance spectroscopy (EIS). Fig. 5b shows the EIS spectra of  $\text{Fe}_2\text{O}_3$ ,  $\text{Fe}_2\text{O}_3$  (LV) and P- $\text{Fe}_2\text{O}_3$  (LV) at 1.23 V (vs. RHE). The fitted parameters of the EIS spectra are shown in Table S1. The  $R_{\text{ct}}$  value represents the surface charge transfer resistance [50]. It is clear that  $R_{\text{ct}}$  for  $\text{Fe}_2\text{O}_3$  (LV) is similar to that for  $\text{Fe}_2\text{O}_3$  (around 200  $\Omega$ ), while the  $R_{\text{ct}}$  value for P- $\text{Fe}_2\text{O}_3$  (LV) significantly decreases to 50  $\Omega$  suggesting the reduced surface charge transfer resistance. The smaller semicircle diameter for P- $\text{Fe}_2\text{O}_3$  (LV) also confirms the faster surface charge transfer. The surface charge recombination can thus be suppressed and the PEC performance can be improved.

Further doping can also be coupled with  $\text{Fe}_2\text{O}_3$  (LV) to enhance the PEC performance due to the favorable intrinsic modifications. Various metal elements have been tested and the Hf-based modification was found to effectively enhance the light absorption efficiency of the pristine  $\text{Fe}_2\text{O}_3$ , as shown in Fig. 5d. The Hf-treated  $\text{Fe}_2\text{O}_3$  (Hf- $\text{Fe}_2\text{O}_3$ ) shows an increased photocurrent of 1.59  $\text{mA}/\text{cm}^2$  at 1.23 V vs. RHE (Fig. 5c) when compared to the pristine  $\text{Fe}_2\text{O}_3$ . Due to the favorable intrinsic modification of oxygen vacancy and  $\beta$ - $\text{Fe}_2\text{O}_3$ , the Hf-modification can be well coupled to further enhance the PEC performance. The detailed Hf-treatment can be found in the experimental section and Fig. S7. The TEM mapping in Fig. S8 confirms the successful Hf-doping in hematite. XRD data in Fig. S8 also shows the presence of  $\beta$ - $\text{Fe}_2\text{O}_3$ . XPS and XAS spectra in Fig. S9 reveal the existence of both Hf and oxygen vacancies in Hf- $\text{Fe}_2\text{O}_3$  (LV). As shown in Fig. 5d, the Hf- $\text{Fe}_2\text{O}_3$  (LV) sample shows an enhanced light absorption efficiency in a broad wavelength range from 420 to 600 nm when compared to the pristine  $\text{Fe}_2\text{O}_3$  (similar to that of Hf- $\text{Fe}_2\text{O}_3$ ). The enhanced light absorption efficiency might be attributed to the Hf-doping induced band gap narrowing as shown in Fig. S9e. As a result, the photocurrent of Hf- $\text{Fe}_2\text{O}_3$  (LV) with better light absorption efficiency can achieve a high photocurrent of 3.69  $\text{mA}/\text{cm}^2$  at 1.23 V vs. RHE in Fig. 5c, which is more than 4 times of that for the pristine  $\text{Fe}_2\text{O}_3$  (0.82  $\text{mA}/\text{cm}^2$ ). The M-S plots of Hf- $\text{Fe}_2\text{O}_3$  and Hf- $\text{Fe}_2\text{O}_3$  (LV) are shown in Fig. S10a, revealing the increased carrier density ( $3.41 \times 10^{21} \text{ cm}^{-3}$ ) in Hf- $\text{Fe}_2\text{O}_3$  (LV) with both oxygen vacancy and  $\beta$ - $\text{Fe}_2\text{O}_3$ . Fig. S10b shows the corresponding EIS curves and the fitting parameters are shown in Table S1. Interestingly, the Hf-treatment can also partly reduce the surface resistance with a small  $R_{\text{ct}}$  value of 183  $\Omega$ . Fig. S11 shows the surface and bulk charge separation efficiencies ( $\eta_{\text{surf}}$  and  $\eta_{\text{bulk}}$ ), suggesting the improved charge separation efficiencies with oxygen vacancy and  $\beta$ - $\text{Fe}_2\text{O}_3$ . The PEC performance of Hf- $\text{Fe}_2\text{O}_3$  (LV) is also very stable as shown in Fig. S12.

The Hf and P based treatments can be easily coupled together with oxygen vacancy and  $\beta$ - $\text{Fe}_2\text{O}_3$  to form the P-Hf- $\text{Fe}_2\text{O}_3$  (LV) sample (the performance is optimized as shown in Fig. S13), which exhibits a high photocurrent of 4.40  $\text{mA}/\text{cm}^2$  at 1.23 V vs. RHE in Fig. 5e. The TEM elemental mappings of P-Hf- $\text{Fe}_2\text{O}_3$  (LV) are shown in Fig. S14 and the corresponding elemental analysis is shown in Fig. S15, confirming the existence of both Hf and P in P-Hf- $\text{Fe}_2\text{O}_3$  (LV). Moreover, by adding the well-known surface co-catalyst of FeNiOOH to accelerate the OER kinetics [52,53], the photocurrent of FeNiOOH-P-Hf- $\text{Fe}_2\text{O}_3$  (LV) can achieve an excellent value of 5.24  $\text{mA}/\text{cm}^2$  at 1.23 V vs. RHE in Fig. 5e, representing one of the highest values for hematite-based photoanodes. A comparison of the performance with those reported in the literature can be found in Table S2 and Fig. 5g. It strongly suggests the potential of  $\text{Fe}_2\text{O}_3$  (LV) as an excellent starting material to achieve high PEC

performance for practical solar water splitting. Fig. 5f shows the EIS spectra of Hf- $\text{Fe}_2\text{O}_3$  (LV), P-Hf- $\text{Fe}_2\text{O}_3$  (LV), and FeNiOOH-P-Hf- $\text{Fe}_2\text{O}_3$  (LV). The semicircle diameter for FeNiOOH-P-Hf- $\text{Fe}_2\text{O}_3$  (LV) is very small, suggesting the fast surface charge transfer with the FeNiOOH co-catalyst. The fitted  $R_{\text{ct}}$  value for FeNiOOH-P-Hf- $\text{Fe}_2\text{O}_3$  (LV) in Table S1 also significantly decreases, revealing the enhanced OER kinetics at the solid/liquid interface.

The high photocurrent density has been justified by performing the chopped  $J$ -V and  $J$ -t curves in Fig. S16. It is clear that the FeNiOOH-P-Hf- $\text{Fe}_2\text{O}_3$  (LV) photoanode can keep the high performance in both the chopped  $J$ -V and  $J$ -t curves under AM 1.5 G chopped illumination. A prolonged electrolysis of FeNiOOH-P-Hf- $\text{Fe}_2\text{O}_3$  (LV) at 1.23 V vs. RHE has also been performed for over 100 h, as shown in Fig. S17. The high photocurrent density around 5.24  $\text{mA}/\text{cm}^2$  is stable in a long working time of 100 h, suggesting the excellent durability. After the stability test,  $J$ -V curve of the used FeNiOOH-P-Hf- $\text{Fe}_2\text{O}_3$  (LV) was measured again, which showed similar performance as that for the fresh sample in Fig. S17. To further confirm the high efficiency of FeNiOOH-P-Hf- $\text{Fe}_2\text{O}_3$  (LV), time-profiled evolutions of  $\text{O}_2$  and  $\text{H}_2$  (FeNiOOH-P-Hf- $\text{Fe}_2\text{O}_3$  (LV) as the photoanode, at 1.23 V vs. RHE) are shown in Fig. 6b [54]. The corresponding photocurrent profiles are also shown.  $\text{O}_2$  can be clearly observed from the hematite photoanode in the PEC process (image not shown). The produced gases of  $\text{H}_2$  and  $\text{O}_2$  were identified by a gas chromatograph. The ratio of produced  $\text{O}_2$  and  $\text{H}_2$  is around 1:2, confirming the water splitting process. According to the measured amounts of produced  $\text{O}_2$  and  $\text{H}_2$ , the Faradaic efficiencies can thus be calculated as shown in Fig. S18, which are around 95% in the whole process [54]. The Faradaic efficiencies of the photoanode after 100 h stability test are shown in Fig. S18, which can keep similar values. XPS, XRD and HRTEM characterizations of  $\text{Fe}_2\text{O}_3$  (LV) after 100 h test are also provided in Fig. S19, which show very similar results to that before the stability test suggesting the stable structure of  $\text{Fe}_2\text{O}_3$  (LV).

The high PEC performance of FeNiOOH-P-Hf- $\text{Fe}_2\text{O}_3$  (LV) can thus be used to realize the practical solar water splitting. A commercial Si solar cell has been directly connected to the hematite photoanode to form a tandem system, as illustrated in Fig. 6a (in a two-electrode configuration). Sunlight has been used as the sole energy source for the system to produce hydrogen. The parameters of commercial Si solar cell have been shown in the experimental section, with an open-circuit voltage ( $V_{\text{oc}}$ ) of 1.276 V and a power conversion efficiency (PCE) of 7.35%. The solar cell alone is unable to directly drive the electrocatalysis for hydrogen production due to the low  $V_{\text{oc}}$ . However, it can work together with the hematite photoanode for efficient solar water splitting. The  $J$ -V curves of both solar cell and hematite photoanode in the tandem system are shown in Fig. 6c. The working current density in the tandem system is around 4.7  $\text{mA}/\text{cm}^2$  (at 1.18 V). Then the STH conversion efficiency can be calculated to be 5.3% for the tandem system (see experimental section). To the best of our knowledge, it is the highest STH value obtained for hematite-based tandem systems for solar water splitting, as also compared in Table. S3.

The working mechanism of FeNiOOH-P-Hf- $\text{Fe}_2\text{O}_3$  (LV) is also illustrated in Fig. 6d. The synthesis of pure  $\beta$ - $\text{Fe}_2\text{O}_3$  has been reported [27, 55], but  $\beta$ - $\text{Fe}_2\text{O}_3$  itself is not a good photoanode for solar water splitting [27]. Actually, in this work the improved PEC performance should be mainly attributed to the synergistic effect of  $\beta$ - $\text{Fe}_2\text{O}_3$  and oxygen vacancy in hematite. Oxygen vacancy can increase the carrier densities and then improve the charge transport. The hetero phase domains in hematite will create abundant interfacial structures, which are favorable for the formation of oxygen vacancies [22]. Moreover, the interfacial structures can release internal stress to reduce the bulk (and/or near surface) defects along with the formation of oxygen vacancies. Thus the internal structure of hematite can be optimized with less defects. As a result, it can significantly improve the bulk charge utilization, which will enhance the charge extraction capability to produce more photo-generated pairs, facilitate the charge transport from bulk to surface, and then suppress the bulk electron-hole recombination with better

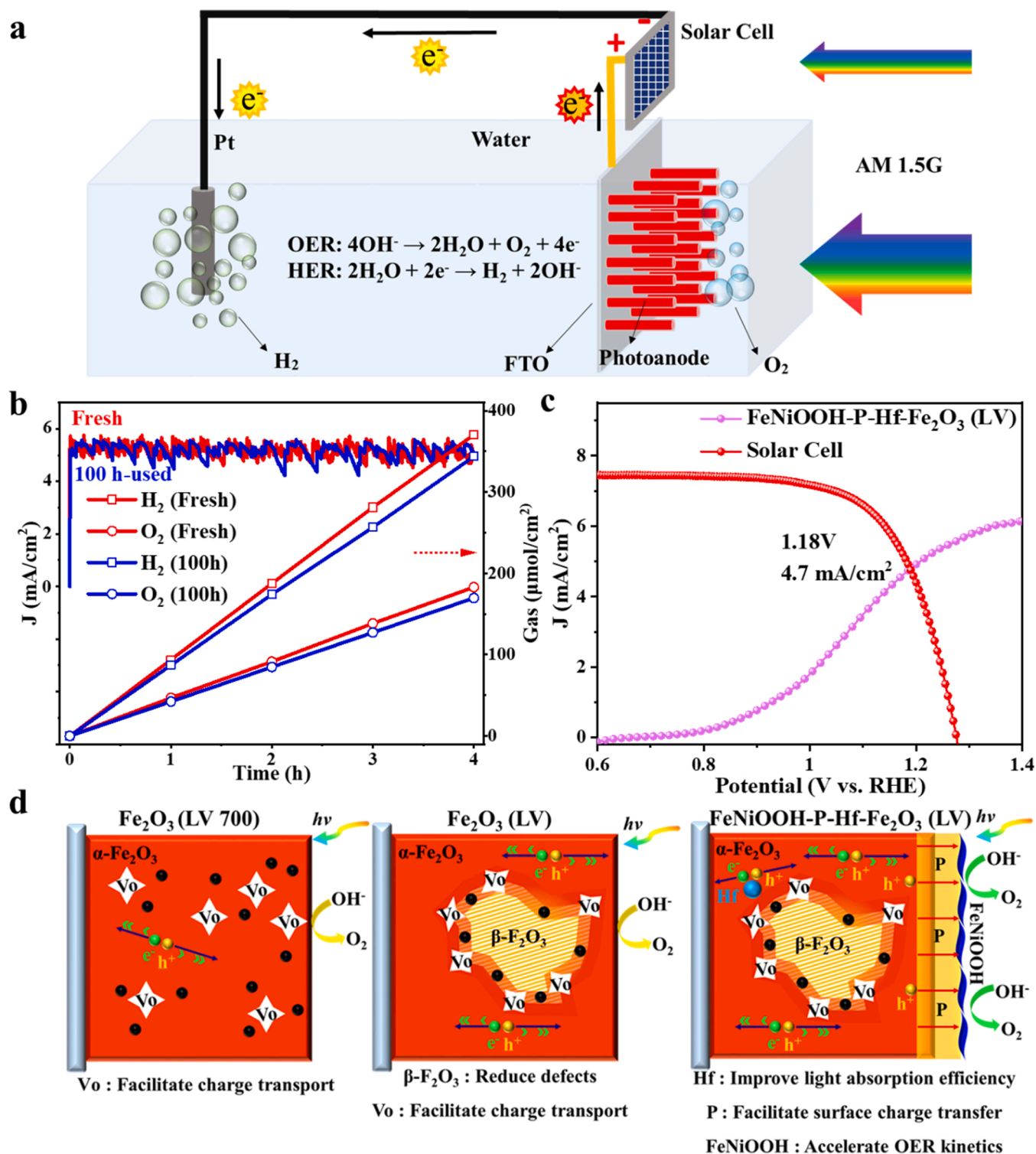


**Fig. 6.** Tandem system with solar cell and the working mechanism. (a) Demonstration of the tandem system for hematite photoanode connected to a commercial Si solar cell. (b) Time-profiled evolutions of  $\text{O}_2$  and  $\text{H}_2$  using  $\text{FeNiOOH-P-Hf-Fe}_2\text{O}_3$  (LV) (as-synthesized and used for 100 h) at 1.23 V vs. RHE. The photocurrent profiles are also shown. (c) J-V curves of solar cell and hematite photoanode together in the tandem system. (d) Schematic diagram of the working mechanism for  $\text{FeNiOOH-P-Hf-Fe}_2\text{O}_3$  (LV).

charge separation efficiency. Due to the favorable intrinsic modifications, the sample can also be well coupled with various modifications, such as P-treatment to facilitate the surface charge transfer, Hf-treatment to improve the light absorption efficiency, and surface  $\text{FeNiOOH}$  co-catalyst to accelerate the OER kinetics. All the above treatments can be positively accumulated to obtain a high photocurrent

of  $5.24 \text{ mA}/\text{cm}^2$  at 1.23 V vs. RHE, which can thus be applied in an easy tandem system to achieve the benchmark STH efficiency of 5.3% for practical solar water splitting.

## 4. Conclusions

The hematite sample with oxygen vacancy and  $\beta\text{-Fe}_2\text{O}_3$  has been prepared by controlling the pressure and temperature in a hydrothermal method. With the synergistic effect of  $\beta\text{-Fe}_2\text{O}_3$  and oxygen vacancy, the bulk charge transport in hematite can be improved and the electron-hole recombination has been suppressed, along with enhanced charge extraction capability. As a result, the photoelectrochemical performance can be significantly improved to obtain a high photocurrent of  $2.72\text{ mA/cm}^2$  at  $1.23\text{ V}$  vs. RHE. It can be further coupled with various modifications such as P-treatment, Hf-treatment, and  $\text{FeNiOOH}$  co-catalyst to achieve an excellent photocurrent of  $5.24\text{ mA/cm}^2$  at  $1.23\text{ V}$  vs. RHE. The photoanode exhibits a good stability over  $100\text{ h}$  with the Faradaic efficiencies around  $95\%$ . Based on the high performance, it can be directly connected to a commercial solar cell to form a tandem system for practical solar water splitting, which can achieve a benchmark STH value of  $5.3\%$ .

## CRediT authorship contribution statement

**Cheng Lu:** Data curation, Visualization. **Duo Zhang:** Investigation. **Zhenyu Wu:** Investigation. **Xiaoquan Zhao:** Formal analysis. **Kun Feng:** Formal analysis. **Gaoteng Zhang:** Software. **Shuao Wang:** Investigation. **Zhenhui Kang:** Conceptualization, Funding acquisition, Writing – review & editing, Supervision. **Jun Zhong:** Writing – review & editing, Supervision.

## Declaration of Competing Interest

The authors declare that they have no known competing financial interests or personal relationships that could have appeared to influence the work reported in this paper.

## Data Availability

Data will be made available on request.

## Acknowledgments

We acknowledge the support from Shanghai Synchrotron Radiation Facility (SSRF, 11B) and the National Synchrotron Radiation Laboratory (NSRL, Beamlines MCD-A and MCD-B (Soochow Beamline for Energy Materials)) for the XAS experiments. This work is supported by the National Key Research and Developmental Program of China (2020YFA0406103, 2020YFA0406104, 2020YFA0406101), the National Natural Science Foundation of China (U1932211, 51725204, 51972216, 52272043, 52271223, 52202107, 52201269), Natural Science Foundation of Jiangsu Province (BK20220028, BK20190041, BK20210735, 21KJB430043), Innovative Research Group Project of the National Natural Science Foundation of China (51821002), Collaborative Innovation Center of Suzhou Nano Science & Technology, the Priority Academic Program Development of Jiangsu Higher Education Institutions (PAPD), the 111 Project and Suzhou Key Laboratory of Functional Nano & Soft Materials.

## Appendix A. Supporting information

Supplementary data associated with this article can be found in the online version at [doi:10.1016/j.apcatb.2023.122695](https://doi.org/10.1016/j.apcatb.2023.122695).

## References

- [1] H. Lan, Y. Xia, K. Feng, A. Wei, Z. Kang, J. Zhong, Co-doped carbon layer to lower the onset potential of hematite for solar water oxidation, *Appl. Catal. B: Environ.* 258 (2019), 117962.
- [2] X.T. Xu, L. Pan, X. Zhang, L. Wang, J.J. Zou, Rational design and construction of cocatalysts for semiconductor-based photo-electrochemical oxygen evolution: a comprehensive review, *Adv. Sci.* 6 (2019) 1801505.
- [3] P.Y. Tang, L.J. Han, F.S. Hegner, P. Paciok, M. Biset-Peiró, H.C. Du, X.K. Wei, L. Jin, H.B. Xie, Q. Shi, T. Andreu, M. Lira-Cantú, M. Heggen, R.E. Dunin-Borkowski, N. López, J.R. Galán-Mascarós, J.R. Morante, J. Arbiol, Boosting photoelectrochemical water oxidation of hematite in acidic electrolytes by surface state modification, *Adv. Energy Mater.* 9 (2019) 1901836.
- [4] T. Jiao, C. Lu, D. Zhang, K. Feng, S. Wang, Z. Kang, J. Zhong, Bi-functional  $\text{Fe}_2\text{ZrO}_5$  modified hematite photoanode for efficient solar water splitting, *Appl. Catal. B: Environ.* 269 (2020), 118768.
- [5] X. Wang, W. Gao, Z. Zhao, L. Zhao, J.P. Claverie, X. Zhang, J. Wang, H. Liu, Y. Sang, Efficient photo-electrochemical water splitting based on hematite nanorods doped with phosphorus, *Appl. Catal. B: Environ.* 248 (2019) 388–393.
- [6] K. Sivula, F.L. Formai, M. Grätzel, Solar water splitting: progress using hematite ( $\alpha\text{-Fe}_2\text{O}_3$ ) photoelectrodes, *ChemSusChem* 4 (2011) 432–449.
- [7] A.G. Tamir, J. Rick, A.A. Dubale, W.N. Su, B.J. Hwang, Using hematite for photoelectrochemical water splitting: a review of current progress and challenges, *Nanoscale Horiz.* 1 (2016) 243–267.
- [8] S. Zhang, Z. Liu, D. Chen, W. Yan, An efficient hole transfer pathway on hematite integrated by ultrathin  $\text{Al}_2\text{O}_3$  interlayer and novel  $\text{CuCoO}_x$  cocatalyst for efficient photoelectrochemical water oxidation, *Appl. Catal. B: Environ.* 277 (2020), 119197.
- [9] C. Feng, S. Fu, W. Wang, Y. Zhang, Y. Bi, High-crystalline and high-aspect-ratio hematite nanotube photoanode for efficient solar water splitting, *Appl. Catal. B: Environ.* 257 (2019), 117900.
- [10] K.Y. Yoon, J. Park, M. Jung, S.G. Ji, H. Lee, J.H. Seo, M.J. Kwak, S.I. Seok, J.H. Lee, J.H. Yang,  $\text{NiFeO}_x$  decorated Ge-hematite/perovskite for an efficient water splitting system, *Nat. Commun.* 12 (2021) 4309.
- [11] T.P. Ruoko, A. Hiltunen, T. Iivonen, R. Ulkuniemi, K. Lahtonen, H. Ali-Löytty, K. Mizohata, M. Valden, M. Leskelä, N.V. Tkachenko, Charge carrier dynamics in tantalum oxide overlayers and tantalum doped hematite photoanodes, *J. Mater. Chem. A* 7 (2019) 3206–3215.
- [12] B.J. Rani, R. Ravi, R. Yuvakkumar, S. Ravichandran, F. Ameen, S. AlNadhy, Sn doped  $\alpha\text{-Fe}_2\text{O}_3$  ( $\text{Sn}=0, 10, 20, 30\text{ wt\%}$ ) photoanodes for photoelectrochemical water splitting applications, *Renew. Energy* 133 (2019) 566–574.
- [13] F. Li, J. Li, L. Gao, Y. Hu, X. Long, S. Wei, C. Wang, J. Jin, J. Ma, Construction of an efficient hole migration pathway on hematite for efficient photoelectrochemical water oxidation, *J. Mater. Chem. A* 6 (2018) 23478–23485.
- [14] A.G. Hufnagel, H. Hajiyani, S. Zhang, T. Li, O. Kasian, B. Gault, B. Breitbach, T. Bein, D. Fattakhova-Rohlfing, C. Scheu, R. Pentcheva, Why tin-doping enhances the efficiency of hematite photoanodes for water splitting—the full picture, *Adv. Funct. Mater.* 28 (2018) 1804472.
- [15] M. Li, Y. Yang, Y. Ling, W. Qiu, F. Wang, T. Liu, Y. Song, X. Liu, P. Fang, Y. Tong, Y. Li, Morphology and doping engineering of Sn-doped hematite nanowire photoanodes, *Nano Lett.* 17 (2017) 2490–2495.
- [16] Y. Ling, G. Wang, D.A. Wheeler, J.Z. Zhang, Y. Li, Sn-doped hematite nanostructures for photoelectrochemical water splitting, *Nano Lett.* 11 (2011) 2119–2125.
- [17] R. Chong, Y. Du, Z. Chang, Y. Jia, Y. Qiao, S. Liu, Y. Liu, Y. Zhou, D. Li, 2D Co-incorporated hydroxyapatite nanoarchitecture as a potential efficient oxygen evolution cocatalyst for boosting photoelectrochemical water splitting on  $\text{Fe}_2\text{O}_3$  photoanode, *Appl. Catal. B: Environ.* 250 (2019) 224–233.
- [18] Y. Ling, G. Wang, J. Reddy, C. Wang, J.Z. Zhang, Y. Li, The influence of oxygen content on the thermal activation of hematite nanowires, *Angew. Chem. Int. Ed.* 51 (2012) 4074–4079.
- [19] M. Forster, R.J. Potter, Y. Ling, Y. Yang, D.R. Klug, Y. Li, A.J. Cowan, Oxygen deficient  $\alpha\text{-Fe}_2\text{O}_3$  photoelectrodes: a balance between enhanced electrical properties and trap-mediated losses, *Chem. Sci.* 6 (2015) 4009–4016.
- [20] J. Moir, N. Soheilnia, K. Liao, P. O'Brien, Y. Tian, K.S. Burch, G.A. Ozin, Activation of ultrathin films of hematite for photoelectrochemical water splitting via  $\text{H}_2$  treatment, *ChemSusChem* 8 (2015) 1557–1567.
- [21] A. Pu, J. Deng, M. Li, J. Gao, H. Zhang, Y. Hao, J. Zhong, X. Sun, Coupling Ti-doping and oxygen vacancies in hematite nanostructures for solar water oxidation with high efficiency, *J. Mater. Chem. A* 2 (2014) 2491–2497.
- [22] Z. Zhang, I. Karimata, H. Nagashima, S. Muto, K. Ohara, K. Sugimoto, T. Tachikawa, Interfacial oxygen vacancies yielding long-lived holes in hematite mesocrystal-based photoanodes, *Nat. Commun.* 10 (2019) 4832.
- [23] M. Li, J. Deng, A. Pu, P. Zhang, H. Zhang, J. Gao, Y. Hao, J. Zhong, X. Sun, Hydrogen-treated hematite nanostructures with low onset potential for highly efficient solar water oxidation, *J. Mater. Chem. A* 2 (2014) 6727–6733.
- [24] Z.Y. Wang, H.M. Li, S.S. Yi, M.Z. You, H.J. Jing, X.Z. Yue, Z.T. Zhang, D.L. Chen, In-situ coating of multifunctional  $\text{FeCo}$ -bimetal organic framework nanolayers on hematite photoanode for superior oxygen evolution, *Appl. Catal. B: Environ.* 297 (2021), 120406.
- [25] L.K. Dhandole, T.S. Koh, P. Anushkaran, H.S. Chung, W.S. Chae, H.H. Lee, S. H. Choi, M. Cho, J.S. Jang, Enhanced charge transfer with tuning surface state in hematite photoanode integrated by niobium and zirconium co-doping for efficient photoelectrochemical water splitting, *Appl. Catal. B: Environ.* 315 (2022), 121538.
- [26] H.M. Li, Z.Y. Wang, H.J. Jing, S.S. Yi, S.X. Zhang, X.Z. Yue, Z.T. Zhang, H.X. Lu, D. L. Chen, Synergetic integration of passivation layer and oxygen vacancy on hematite nanoarrays for boosted photoelectrochemical water oxidation, *Appl. Catal. B: Environ.* 284 (2021), 119760.
- [27] Y. Li, N. Zhang, C. Liu, Y. Zhang, X. Xu, W. Wang, J. Feng, Z. Li, Z. Zou, Metastable-phase  $\beta\text{-Fe}_2\text{O}_3$  photoanodes for solar water splitting with durability exceeding  $100\text{ h}$ , *Chin. J. Catal.* 42 (2021) 1992–1998.



- [28] Y. Chen, Z. Lai, X. Zhang, Z. Fan, Q. He, C. Tan, H. Zhang, Phase engineering of nanomaterials, *Nat. Rev. Chem.* 4 (2020) 243–256.
- [29] L. Vayssieres, N. Beermann, S.E. Lindquist, A. Hagfeldt, Controlled aqueous chemical growth of oriented three-dimensional crystalline nanorod arrays: application to iron(III) oxides, *Chem. Mater.* 13 (2001) 233–235.
- [30] J. Deng, X. Lv, H. Zhang, B. Zhao, X. Sun, J. Zhong, Phys. Loading the FeNiOOH cocatalyst on Pt-modified hematite nanostructures for efficient solar water oxidation, *Phys. Chem. Chem. Phys.* 18 (2016) 10453–10458.
- [31] Y. Makimizu, J.E. Yoo, M. Poornajar, N.T. Nguyen, H.J. Ahn, I. Hwang, S. Kmentc, P. Schmuki, Effects of low oxygen annealing on the photoelectrochemical water splitting properties of  $\alpha$ -Fe<sub>2</sub>O<sub>3</sub>, *J. Mater. Chem. A* 8 (2020) 1315–1325.
- [32] T.H. Jeon, A.D. Bokare, D.S. Han, A. Abdel-Wahab, H. Park, W. Choi, Dual modification of hematite photoanode by Sn-doping and Nb<sub>2</sub>O<sub>5</sub> layer for water oxidation, *Appl. Catal. B: Environ.* 201 (2017) 591–599.
- [33] Y. Ling, G. Wang, H. Wang, Y. Yang, Y. Li, Low-temperature activation of hematite nanowires for photoelectrochemical water oxidation, *ChemSusChem* 7 (2014) 848–853.
- [34] Y. Ye, J.E. Thorne, C.H. Wu, Y.S. Liu, C. Du, J.W. Jang, E. Liu, D. Wang, J. Guo, Strong O 2p-Fe 3d hybridization observed in solution-grown hematite films by soft X-ray spectroscopies, *J. Phys. Chem. B* 122 (2018) 927–932.
- [35] S. Shen, J. Zhou, C.L. Dong, Y. Hu, E.N. Tseng, P. Guo, L. Guo, S.S. Mao, Surface engineered doping of hematite nanorod arrays for improved photoelectrochemical water splitting, *Sci. Rep.* 4 (2014) 6627.
- [36] F.M.F. de Groot, M. Grioni, J.C. Fuggle, J. Ghijsen, G.A. Sawatzky, H. Petersen, Oxygen 1s x-ray-absorption edges of transition-metal oxides, *Phys. Rev. B* 40 (1989) 5715–5723.
- [37] J. Deng, Q. Zhang, X. Lv, D. Zhang, H. Xu, D. Ma, J. Zhong, Understanding photoelectrochemical water oxidation with X-ray absorption spectroscopy, *ACS Energy Lett.* 5 (2020) 975–993.
- [38] F. Frati, M.O.J.Y. Hunault, F.M.F. de Groot, Oxygen K-edge X-ray absorption spectra, *Chem. Rev.* 120 (2020) 4056–4110.
- [39] Z.Y. Wu, G. Ouvrard, P. Gressier, C.R. Natoli, Ti and O K edges for titanium oxides by multiple scattering calculations: comparison to XAS and EELS spectra, *Phys. Rev. B* 55 (1997) 10382–10391.
- [40] D. Cibrev, M. Tallarida, C. Das, T. Lana-Villarreal, D. Schmeisser, R. Gomez, New insights into water photooxidation on reductively pretreated hematite photoanodes, *Phys. Chem. Chem. Phys.* 19 (2017) 21807–21817.
- [41] S.S. Mao, S. Shen, L. Guo, Nanomaterials for renewable hydrogen production, storage and utilization, *Prog. Nat. Sci.* 22 (2012) 522–534.
- [42] S.S. Yi, J.M. Yan, Q. Jiang, Carbon quantum dot sensitized integrated Fe<sub>2</sub>O<sub>3</sub>@g-C<sub>3</sub>N<sub>4</sub> core-shell nanoarray photoanode towards highly efficient water oxidation, *J. Mater. Chem. A* 6 (2018) 9839–9845.
- [43] Z. Zhou, J. Liu, R. Long, L. Li, L. Guo, O.V. Prezhdo, Control of charge carriers trapping and relaxation in hematite by oxygen vacancy charge: Ab initio non-adiabatic molecular dynamics, *J. Am. Chem. Soc.* 139 (2017) 6707–6717.
- [44] Z. Zhang, H. Nagashima, T. Tachikawa, Ultra-narrow depletion layers in a hematite mesocrystal-based photoanode for boosting multihole water oxidation, *Angew. Chem. Int. Ed.* 59 (2020) 9047–9054.
- [45] Z. Wang, X. Mao, P. Chen, M. Xiao, S.A. Monny, S. Wang, M. Konarova, A. Du, L. Wang, Understanding the roles of oxygen vacancies in hematite-based photoelectrochemical processes, *Angew. Chem. Int. Ed.* 58 (2019) 1030–1034.
- [46] Z.Y. Wu, X.T. Wang, Y. Li, H. Zhao, J.W. Wang, H. Huang, Y. Liu, Z.H. Kang, Converting water impurity in organic solvent into hydrogen and hydrogen peroxide by organic semiconductor photocatalyst, *Appl. Catal. B: Environ.* 305 (2022), 121047.
- [47] W.S. Jiang, Y.J. Zhao, X.P. Zong, H.D. Nie, L.J. Niu, L. An, D. Qu, X.Y. Wang, Z. H. Kang, Z.C. Sun, Photocatalyst for high-performance H<sub>2</sub> production: Ga-doped polymeric carbon nitride, *Angew. Chem. Int. Ed.* 60 (2021) 6124–6129.
- [48] Z. Luo, C. Li, S. Liu, T. Wang, J. Gong, Gradient doping of phosphorus in Fe<sub>2</sub>O<sub>3</sub> nanoarray photoanodes for enhanced charge separation, *Chem. Sci.* 8 (2017) 91–100.
- [49] Y. Zhang, S. Jiang, W. Song, P. Zhou, H. Ji, W. Ma, W. Hao, C. Chen, J. Zhao, Nonmetal P-doped hematite photoanode with enhanced electron mobility and high water oxidation activity, *Energy Environ. Sci.* 8 (2015) 1231–1236.
- [50] Y. Zhang, Z. Zhou, C. Chen, Y. Che, H. Ji, W. Ma, J. Zhang, D. Song, J. Zhao, Gradient FeO<sub>x</sub>(PO<sub>4</sub>)<sub>y</sub> layer on hematite photoanodes: novel structure for efficient light-driven water oxidation, *ACS Appl. Mater. Inter.* 6 (2014) 12844–12851.
- [51] X. Lv, K. Nie, H. Lan, X. Li, Y. Li, X. Sun, J. Zhong, S.T. Lee, Fe<sub>2</sub>TiO<sub>5</sub>-incorporated hematite with surface P-modification for high-efficiency solar water splitting, *Nano Energy* 32 (2017) 526–532.
- [52] S. Shen, S.A. Lindley, X. Chen, J.Z. Zhang, Hematite heterostructures for photoelectrochemical water splitting: rational materials design and charge carrier dynamics, *Energy Environ. Sci.* 9 (2016) 2744–2775.
- [53] J. Deng, Q. Zhang, K. Feng, H. Lan, J. Zhong, M. Chaker, D. Ma, Efficient photoelectrochemical water oxidation on hematite with fluorine-doped FeOOH and FeNiOOH as dual cocatalysts, *Chemsuschem* 11 (2018) 3783–3789.
- [54] T.H. Jeon, G.H. Moon, H. Park, W. Choi, Ultra-efficient and durable photoelectrochemical water oxidation using elaborately designed hematite nanorod arrays, *Nano Energy* 39 (2017) 211–218.
- [55] N. Zhang, Y. Guo, X. Wang, S. Zhang, Z. Li, Z. Zou, A beta-Fe<sub>2</sub>O<sub>3</sub> nanoparticle-assembled film for photoelectrochemical water splitting, *Dalton Trans.* 46 (2017) 10673–10677.